Research Article

For reprint orders, please contact: reprints@futuremedicine.com

Nanomedicine

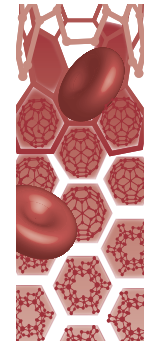

Peptide conjugated magnetic nanoparticles for magnetically mediated energy delivery to lung cancer cells

Anastasia K Hauser[1], Kimberly W Anderson[1] & J Zach Hilt*[,1]

[1]Department of Chemical & Materials Engineering, University of Kentucky, Lexington, KY 40506, USA

*Author for correspondence:
Tel.: +1 859 257 9844
Fax: +1 859 323 1929
hilt@engr.uky.edu

Aim: In the present study, we examine the effects of internalized peptide-conjugated iron oxide nanoparticles and their ability to locally convert alternating magnetic field (AMF) energy into other forms of energy (e.g., heat and rotational work). **Materials & methods:** Dextran-coated iron oxide nanoparticles were functionalized with a cell penetrating peptide and after internalization by A549 and H358 cells were activated by an AMF. **Results:** TAT-functionalized nanoparticles and AMF exposure increased reactive oxygen species generation compared with the nanoparticle system alone. The TAT-functionalized nanoparticles induced lysosomal membrane permeability and mitochondrial membrane depolarization, but these effects were not further enhanced by AMF treatment. Although not statistically significant, there are trends suggesting an increase in apoptosis via the Caspase 3/7 pathways when cells are exposed to TAT-functionalized nanoparticles combined with AMF. **Conclusion:** Our results indicate that internalized TAT-functionalized iron oxide nanoparticles activated by an AMF elicit cellular responses without a measurable temperature rise.

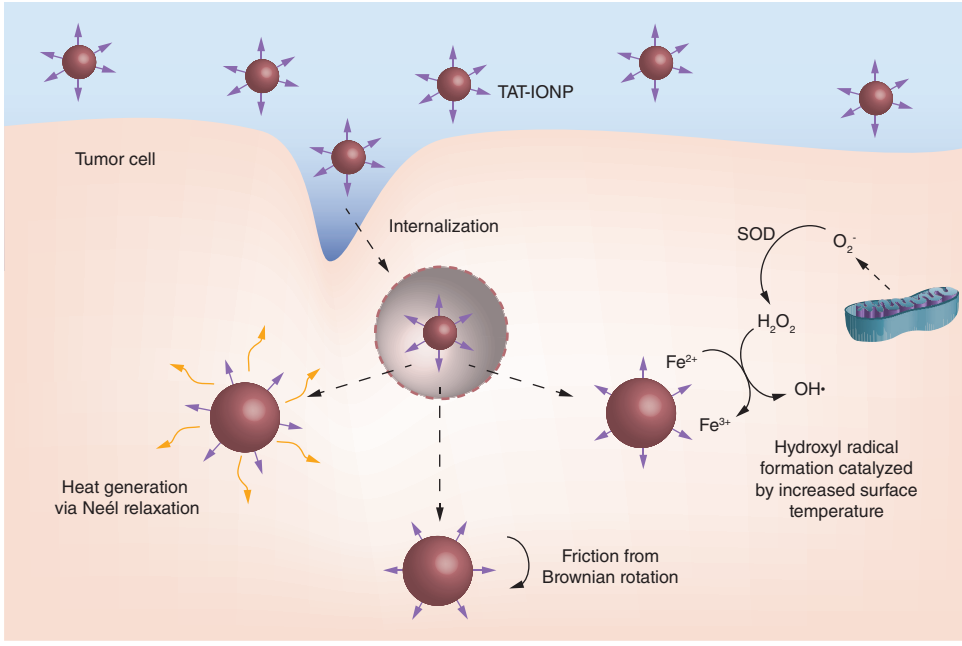

First draft submitted: 12 February 2016; Accepted for publication: 16 May 2016; Published online: 7 July 2016

Keywords: cell penetrating peptide • iron oxide nanoparticles • magnetically medicated energy delivery • reactive oxygen species • TAT

Future Medicine part of fsg

Background

Iron oxide nanoparticles have been studied for a wide variety of biological applications including MRI, magnetic targeting, cell separation techniques, drug delivery, magnetically mediated hyperthermia (MMH) and in the treatment of anemia [1–6]. In MMH, iron oxide nanoparticles convert energy from an alternating magnetic field (AMF) to heat via Neél relaxation and Brownian rotation [4]. MMH targets a bulk temperature rise between 42 and 45°C, which can lead to adverse cellular effects, and although MMH has been extensively studied, its translation into the clinic has been limited. MMH studies completed *in vitro* utilize high bulk nanoparticle concentrations (on the order of mg/ml) to achieve hyperthermia conditions in monolayer cells or cell suspensions [2,7–10], and most *in vivo* experiments directly inject nanoparticles into tumors (usually subcutaneous) due to the need for high local concentrations to generate a bulk temperature rise [11,12]. Since direct injection is not suitable for many tumors and metastases, there is a gap between bench scale MMH studies and clinical relevance.

Instead of relying on a bulk temperature rise to induce hyperthermia conditions, it was suggested by Gordon *et al.* in 1979 that intracellular hyperthermia would be more advantageous due to insulation by the cell membrane and lack of convection from blood flow which dissipates heat away from the tumor tissue. Heat dissipation is especially problematic when treating small metastatic tumors with hyperthermia [13]. Nanoscale heating effects of the nanoparticles have the ability to induce cellular toxicities as shown by Creixell *et al.* in 2011, where internalized iron oxide nanoparticles in the presence of an AMF induced a significant decrease in cell viability without a measurable temperature rise [14]. This phenomena was observed by other groups as well using a manganese oxide nanoparticle system [15] and has been utilized in applications other than cancer therapy, such as therapy against parasite infections [16]. The phrase magnetically mediated energy delivery (MagMED) was then coined to describe the conversion of magnetic field energy to other forms such as heat or rotation work but without significantly increasing the bulk temperature [17].

Although there is a growing body of evidence suggesting that local heating and energy delivery can be used to kill cancer cells, theoretical calculations by Rabin *et al.* indicate that the heat dissipation from the nanoparticle surface through conduction is greater than the heat being generated by the nanoparticles [18]. These theoretical calculations were disputed when Huang *et al.* utilized iron oxide nanoparticles targeted to proteins on the membrane of cells expressing TRPV1 to locally deliver heat and open cation channels [19]. Nanoparticle heating at the surface was confirmed using a tethered thermoresponsive fluorophore which fluoresced almost immediately upon AMF exposure.

In addition to the effects of surface heating of magnetic nanoparticles in an AMF, rotational work has also been studied as an explanation to the experimental effects of MagMED. For example, mechanical forces have been used to induce lysosomal permeabilization [20,21], leading to the release of proteolytic enzymes such as cathepsins which initiate apoptotic pathways [22–24]. This technique has also been shown to stimulate apoptosis in apoptosis-resistant cell lines [25]. Sanchez *et al.* proved that magnetic nanoparticles functionalized with the ligand of a G-protein coupled receptor were uptaken into malignant cancer cells and able to induce apoptosis and cell death through a lysosomal mediated pathway without a measurable temperature rise [20]. Zhang *et al.* developed a dynamic magnetic field generator to induce nanoparticle rotations about their axis to examine whether physical nanoparticle rotations can disrupt lysosomal membranes and induce apoptosis [26]. By functionalizing the nanoparticles with antibodies for the lysosomal protein marker, it was found that the shear forces generated by oscillating torques were enough to damage the lysosomal membranes, proving that Brownian rotation of magnetic nanoparticles also plays an important role in MagMED treatment.

In addition to the thermal and mechanical effects described above, the production of reactive oxygen species (ROS) via iron oxide nanoparticles is a potential chemical effect of MagMED. Iron oxide nanoparticles catalyze the Haber–Weiss reaction which makes use of Fenton chemistry, and this reaction is considered a major mechanism by which the highly reactive hydroxyl radical is generated in biological systems [27]. The Fenton chemistry reaction set is shown as Equation 1 and the Haber–Weiss reaction (net reaction) is shown as Equation 2.

$$Fe^{3+} + O_2^{\bullet -} \rightarrow Fe^{2+} + O_2$$

$$Fe^{2+} + H_2O_2 \rightarrow Fe^{3+} + OH^- + OH\cdot$$

$$O_2^{\bullet -} + H_2O_2 \rightarrow O_2 + OH^- + OH\cdot$$

When iron oxide nanoparticles enter a cell, they can stimulate the generation of ROS via one of the two pathways: the release of ions into the cytosol resulting in the iron ions participating in the Haber–Weiss cycle or the surface of the nanoparticle may act as a catalyst for the Haber–Weiss cycle and the Fenton Reaction [28]. Although this reaction can proceed without the addition of an AMF, recent work by Wydra *et al.*

demonstrated that the reaction is further catalyzed by iron oxide nanoparticles in the presence of an AMF [29].

In order to increase intracellular concentrations of iron oxide nanoparticles and therefore increase the efficacy of MagMED, magnetic nanoparticles can be functionalized with ligands, peptides or antibodies, in order to target and penetrate into the cells. Here, the TAT peptide (sequence: YGRKKRRQRRR) was of particular interest due to its cell penetrating properties and associated ability to avoid receptor mediated endocytosis, as well as its nuclear localizing signal. The TAT peptide contains a characteristic lysine–arginine sequence, and biomolecules with this tag are known to bind to importin-α and -β in the cytoplasm which facilitate active transportation to the nuclear pore complex (NPC) and, if attached to a small enough molecule or particle, through the NPC into the nucleus [30]. The positive charge of the TAT peptide also destabilizes the endosome/lysosome membrane leading to nanoparticle and proteolytic enzyme escape from the vesicles, which plays a role in apoptosis initiation. Previous work by Pan *et al.* in 2012 showed that functionalization of doxorubicin (DOX) loaded silica nanoparticles with the TAT peptide facilitated DOX accumulation within the nuclear membrane [31]. Another study by Austin *et al.* proved that TAT-functionalized silver nanospheres were up taken in to HSC-3 cancer cells at significantly greater concentrations than PEG functionalized nanospheres [30]. Several studies have utilized the TAT peptide as a cell internalization mechanism [32–36] as well as a nuclear targeting moiety [37–41]. Due to the size of our iron oxide nanoparticles being larger than the upper limit of the NPC (20–70 nm), we are interested in using the TAT peptide to escape endosome/lysosomes and facilitate interaction with other organelles such as the mitochondria [31].

In this study, dextran coated iron oxide nanoparticles were functionalized with a cell penetrating peptide, TAT and characterized for their physical and chemical properties. Uptake studies into A549 and H358 non-small-cell lung carcinoma cells indicated that attachment of the TAT peptide to iron oxide nanoparticles significantly increased cell internalization of the nanoparticles. The effects of internalized iron oxide nanoparticles in combination with AMF exposure on A549 and H358 cells were evaluated. Although A549 and H358 are both non-small-cell lung carcinoma cells, this treatment is applicable to a wide variety of cancers, and these cells lines were chosen to assess cell line variability of the treatment. Intracellular generation of ROS, lysosomal membrane permeability, mitochondrial membrane depolarization and apoptosis via the Caspase 3/7 pathway were all evaluated. Finally, cell viability was analyzed to determine the toxicity effects of the treatment. Figure 1 depicts the three main mechanisms by which MagMED can affect cells. After internalization of the TAT conjugated iron oxide nanoparticles, the lysosomal/endosomal membranes were permeabilized and facilitated nanoparticle escape into the cytosol. Upon actuation by an AMF, nanoparticles dissipated energy through Neel relaxations, frictional energy via Brownian rotation and catalyzed ROS generation. All three of these mechanisms can play a role in the efficacy of MagMED.

Materials & methods

Materials

Iron (III) chloride hexahydrate ($FeCl_3 \cdot 6H_2O$), iron (II) chloride ($FeCl_2 \cdot 4H_2O$), 9–11 kDa dextran, epichlorohydrin (ECH) were obtained from Sigma-Aldrich (MO, USA). Ammonium hydroxide (NH_4OH) was purchased from EMD Chemicals (NJ, USA). Phosphate buffered saline solution (PBS) (10×) was purchased from EMD Millipore (MA, USA). The activation buffer 2-[N-morpholino] ethane sulfonic acid (MES), *N*-hydroxysulfosuccinimide (sulfo-NHS) and 1-ethyl-3-[3-dimethylaminopropyl] carbodiimide hydrochloride (EDC) were purchased from Thermo scientific (IL, USA). The TAT peptide was purchased from Biomatik. Phosphate buffered saline (PBS), Dulbecco's Modified Eagle Medium (DMEM), pen-strep, L-glutamine, Fungizone®, sodium pyruvate, CellEvent caspase 3/7 Assay, JC-1 and calcein AM were obtained from Invitrogen (MD, USA). Acridine orange was purchased from Nexcelom Bioscience (MA, USA) and A549 lung carcinoma and trypsin were purchased from American Type Culture Collection (ATCC, VA, USA). All materials were used as received.

Synthesis of uncoated Fe_3O_4 iron oxide nanoparticles

$FeCl_3 \cdot 6H_2O$ and $FeCl_2 \cdot 4H_2O$ were combined in a 2:1 molar ratio (2.2 and 0.8 g, respectively) and dissolved in 60 ml deionized (DI) water and sealed in a three-neck flask under vigorous stirring and an inert nitrogen environment. The reaction solution was heated to 85°C at which 5 ml of 30% NH_4OH was diluted to 40 ml with DI water and the combined solution was injected dropwise into the vessel. The reaction was carried out for 1 h at 85°C. The particles were magnetically decanted and washed three-times with DI water. The nanoparticles were then resuspended in DI water and dialyzed against DI water for 24 h (100 kDa molecular weight cutoff). After dialysis, the nanoparticles were probe sonicated for 10 min and then centrifuged at 1000 rpm for 5 min to remove large agglomerates.

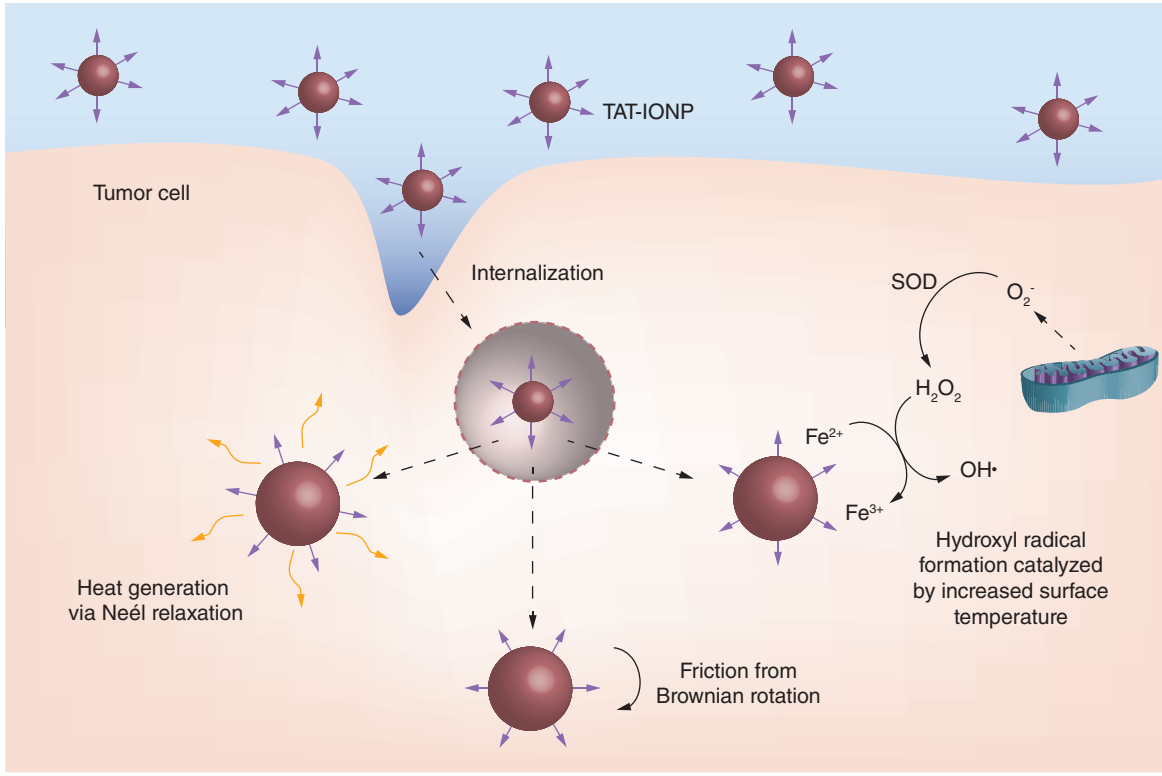

Figure 1. TAT-conjugated iron oxide nanoparticles are internalized by cancer cells and permeabilize endosomal/lysosomal membranes due to the positive charge of the peptide. Upon exposure to an alternating magnetic field, the nanoparticles generate the hydroxyl radical via Fenton chemistry, friction from Brownian rotaion and nanoscale heat effects by Neél relaxation.

Synthesis of dextran coated iron oxide nanoparticles (Fe_3O_4 + Dx)

$FeCl_3 \cdot 6H_2O$ and $FeCl_2 \cdot 4H_2O$ were combined in a 2:1 molar ratio (2.2 and 0.8 g, respectively) and dissolved in 40 ml DI water and sealed in a three-neck flask under vigorous stirring and an inert nitrogen environment. Five grams of dextran was solubilized in 20 ml of DI water. The reaction solution was heated to 85°C at which 5 ml of 30% NH_4OH was added to the dextran solution and the combined solution was injected dropwise into the vessel. The reaction was carried out for 1 h at 85°C. The particles were magnetically decanted and washed three times with DI water. The nanoparticles were then resuspended in DI water and dialyzed against DI water for 24 h (100 kDa molecular weight cutoff). After dialysis, the nanoparticles were probe sonicated for 10 min and then centrifuged at 1000 rpm for 5 min to remove large agglomerates.

Epichlorohydrin (ECH) cross-linking of dextran coated iron oxide nanoparticles (Fe_3O_4 + Dx-ECH)

Dextran coated iron oxide nanoparticles were cross-linked using ECH for increased stability [42]. The particle colloid (9 ml, 1 mmol Fe) was added to 9 ml 5M NaOH and 1.5 ml ECH. The reaction was carried out for 24 h at room temperature under continuous agitation. The particles were then magnetically decanted and dialyzed against DI water (100 kDa molecular weight cutoff) for 24 h to remove excess ECH.

Amine functionalization of crosslinked dextran coated iron oxide nanoparticles (Fe_3O_4 + Dx-ECH-Amine)

An equal volume of ammonium hydroxide to mmol iron from Fe_3O_4 + Dx-ECH were combined and placed on the shaker table for 24 h. After 24 h, the nanoparticles were dialyzed against DI H_2O for an additional 24 h, with their water changed three-times during this time period.

TAT peptide conjugation to iron oxide nanoparticles (Fe_3O_4 + TAT)

Around 10 mg of the TAT-peptide was dissolved in 10 ml MES buffer (2-[N-morpholino] ethane sulfonic acid). Around 4 mg EDC and 11 mg sulfo-NHS were also added to the solution. Solution was reacted for 15 min with continuous agitation after which 14 µl of 2-mercaptoethanol was added to the reaction in order to quench excess EDC. Amine-functionalized iron oxide nanoparticles were diluted to 1 mg Fe_3O_4/

ml with PBS. The iron oxide suspension was added to the TAT-peptide solution and reacted over night under continuous agitation. After the Fe_3O_4 + TAT reaction was complete, and particles were washed with PBS via magnetic decanting until the washing solution was clear. This protocol was adapted from Pan *et al.* [31].

Iron concentration assay

Between each step of synthesizing a new system of iron oxide nanoparticles, an iron assay was used to determine the iron concentration of the nanoparticles. 20×, 50× and 100× dilutions of the iron oxide nanoparticles were made in DI water and 10 µl of each dilution was added to 10 µl 6M HCl and allowed to sit for 3 h. After this time, 500 µl of 1 M acetic acid, 100 µl of hydroxylamine hydrochloride, 100 µl of 1, 10 phenanthroline and 280 µl of DI water were added to each dilution. Solutions were left overnight. After 24 h, the absorbance of each solution (λ = 511 nm) was used to calculate the iron concentration based on a standard curve.

Iron oxide nanoparticle characterization

Dynamic light scattering (DLS)

DLS measurements were obtained using a Beckman Coulter Delsa Nano C particle analyzer Nanoparticle solutions were diluted to 200 µg/ml in DI water or cell culture media and were sonicated in a water bath for 5 min prior to size analysis. The reported nanoparticle sizes in cell culture media were recorded 10 min after bath sonication.

Zeta potential

Zeta potential measurements were obtained using a Beckman Coulter Delsa Nano C particle analyzer. Nanoparticle solutions were diluted to 200 µg/ml in 2 mM NaCl and were sonicated in a water bath prior to analysis.

X-ray diffraction (XRD)

XRD patters were obtained by a Siemens D-500 x-ray spectrometer with a CuKα radiation source (λ = 1.54 Å) at 40 kV and 30 mA scanning from 5° to 65° at a scan rate of 1° per min. The XRD patterns were used to confirm the magnetite crystal structure of the iron oxide nanoparticles. The XRD patterns are in coherence with JDPCS card (19–0629). The crystal domain size was estimated using the Scherrer equation (Equation 3):

$$\tau = \frac{K\lambda}{\beta cos\Theta}$$

where T is the mean size of the ordered (crystalline) domains, K is a dimensionless shape factor with a value close to unity (0.8396 for iron oxide), λ is the x-ray wavelength, β is the line broadening at half the maximum intensity (FWHM) in radians after subtracting the instrumental line broadening and θ is the Bragg angle (17.72°).

Fourier transform infrared spectra

Attenuated total reflectance Fourier transform infrared (FTIR; ATR-FTIR) was used to determine surface functionalization with a Varian Inc. 7000e spectrometer. Dried samples were placed on the diamond ATR crystal and the spectrum was obtained between 700 and 4000 cm^{-1} for 32 scans.

Transmission electron microscopy

Transmission electron microscopy (TEM) was completed using a JEOL 2010F system operating at 200 keV. Dextran coated iron oxide nanoparticles were diluted to 1 mg/ml Fe in DI water and then dried on carbon TEM grids prior to analysis. The TEM images were analyzed using SigmaScan® 5.0 software (Systat, CA, USA) to digitally determine the average crystal size of the iron oxide nanoparticles. At least 60 crystals from ten images were analyzed.

Cell culture

A549 and H358 cells were cultured between passages 5–11 in Dulbecco's modified Eagle medium (DMEM) supplemented with 10% of fetal bovine serum (FBS), 1 mM sodium pyruvate, 4 mM L-glutamine, Pen-Strep (100 µg/ml penicillin and 100 µg/ml streptomycin) and 10 µg/ml of Fungizone. Cells incubated at 37°C and 5% CO_2. A549 are lung carcinoma and H358 are bronchialveolar carcinoma. Both are derived from epithelial cells but the proliferation rates of A549 and H358 cells differ greatly with doubling rates of approximately 22 and 38 h, respectively. This can cause differences in response to treatment as A549 cells have been generally accepted to be more robust and H358 cells more sensitive to treatment. These cell lines were chosen for comparison due to their similar origin but different proliferation properties. These cell lines have been previously compared in literature in a variety of studies [43–46].

Iron oxide nanoparticle uptake

A549 and H358 cells were seeded into 6-well plates at a density of 100,000 cells/ml and 2 ml/well. After 24 h, the spent media was removed and cells were exposed to the nanoparticle systems (uncoated Fe_3O_4, Fe_3O_4 + Dx-ECH or Fe_3O_4 + TAT) at a concentration of 500 µg/ml for 2 h. After 2 h, the nanoparticles were removed and the cells were washed twice with PBS to remove any nanoparticles not internalized within the cells. Cells were then detached from the 6-well plates and counted using a Nexcelom Cellometer to determine the cell

concentration in each well. Cells were then centrifuges and the media supernatant was removed. The cell pellets were dried overnight then dissolved in 6 M HCl for 72 h. After 72 h, 10 µl of the dissolved cell pellet was transferred to a new microcentrifuge tube and the iron concentration assay was completed. The iron concentration was then normalized to the number of cells in the sample.

AMF exposure

A custom made Taylor Winfield magnetic induction source was used for AMF treatment, and the temperature was measured with a fiber optic temperature sensor (Luxtron FOT Lab Kit from LumaSense). One milliliter of cell suspension in a 2 ml sterilized microcentrifuge tube was placed in the center of the AMF induction coil for the stated exposure time (30 min or 1 h). The cell suspension was exposed to a field amplitude of 58 kA/m and frequency of 292 kHz, and the temperature did not increase above 37°C due to the nanoparticles being internalized within the cells and not inducing a bulk thermal effect. The AMF exposure times were selected based on prior work indicating that a 1 h AMF exposure induced enough ROS generation to result in subcellular effects [47].

Reactive oxygen species generation

A549 and H358 cells were seeded at 150,000 cells/ml and 2 ml/well in 6-well plates. After 24 h of growth, the spent media was removed, and the cells were exposed to various nanoparticle systems (uncoated Fe_3O_4, Fe_3O_4 + Dx-ECH or Fe_3O_4 + TAT) at a concentration of 500 µg/ml iron oxide for 2 h. After 2 h of exposure to the nanoparticles, the nanoparticle solutions were removed and cells were washed two-times with PBS, prior to trypsinizing and transferring the cells to microcentrifuge tubes. The cells were then centrifuged and resuspended in 1 ml of 50 µM 6-carboxy-2',7'-dichlorodihydrofluorescein (carboxy-DCF) solution. The cells were incubated in the carboxy-DCF solution for 30 min to facilitate internalization of the dye. Half of the samples were then exposed to an AMF (292 kHz, 56 kA/m) for 30 min or 1 h with 30 min post incubation. Carboxy-DCF fluorescence was measured using an Accuri Flow Cytometer in FL-1.

Acridine orange lysosomal permeabilization experiments

A549 and H358 cells were seeded at 150,000 cells/ml and 2 ml/well into 6-well plates. After 24 h of incubation, the spent media was removed, and cells were exposed to the nanoparticle systems (uncoated Fe_3O_4, Fe_3O_4 + Dx-ECH or Fe_3O_4 + TAT) for 2 h at a concentration of 500 µg/ml iron oxide then rinsed to remove any nanoparticles not associated with the cells. The cells were trypsinized, the trypsin was neutralized with cell culture media and then the cells were transferred to 1.5 ml microcentrifuge tubes. Half the cells were exposed to an AMF (292 kHz, 56 kA/m) for 1 h, then the cells were stained with acridine orange (10 µg/ml) for 10 min at 37°C prior to analysis using an Accuri Flow Cytometer (FL-3).

Mitochondrial membrane depolarization studies (JC-1)

A549 and H358 cells were seeded at 150,000 cells/ml and 2 ml/well into 6-well plates. After 24 h of incubation, the spent media was removed, and cells were exposed to the nanoparticle systems (uncoated Fe_3O_4, Fe_3O_4 + Dx-ECH or Fe_3O_4+TAT) for 2 h at a concentration of 500 µg/ml iron oxide then rinsed to remove any nanoparticles not associated with the cells. The cells were trypsinized, the trypsin was neutralized with cell culture media and then the cells were transferred to 1.5 ml microcentrifuge tubes. Half the cells were exposed to an AMF (292 kHz, 56kA/m) for 1 h, then the cells were centrifuged, resuspended in PBS and stained with JC-1 (2 µM) for 30 min at 37°C prior to analysis using an Accuri Flow Cytometer (FL-1 and FL-3).

Caspase 3/7 apoptosis studies

A549 and H358 cells were seeded at 150,000 cells/ml and 2 ml/well into 6-well plates. After 24 h of incubation, the spent media was removed and cells were exposed to the nanoparticle systems (uncoated Fe_3O_4, Fe_3O_4 + Dx-ECH or Fe_3O_4 + TAT) for 2 h at a concentration of 500 µg/ml iron oxide then rinsed to remove any nanoparticles not associated with the cells. The cells were trypsinized, the trypsin was neutralized with cell culture media and then the cells were transferred to 1.5 ml microcentrifuge tubes. Half the cells were exposed to an AMF (292 kHz, 56 kA/m) for 1 h. At 12 or 24 h post AMF treatment, the cells were centrifuged, resuspended in PBS and stained with CellEvent per manufacturer's instructions (1 µl CellEvent/ml cell solution) for 30 min at 37°C prior to analysis using an Accuri Flow Cytometer (FL-1). Cells were gated into two populations: nonapoptotic and apoptotic, with the apoptotic group being higher in FL-1 fluorescence and decreased in forward scatter.

Viability studies

A549 and H358 cells were seeded at 150,000 cells/ml and 2 ml/well into 6-well plates. After 24 h of incubation, the spent media was removed, and cells were exposed to the nanoparticle systems (uncoated Fe_3O_4, Fe_3O_4 + Dx-ECH or Fe_3O_4 + TAT) for 2 h at a final

concentration of 500 µg/ml iron oxide then rinsed to remove any nanoparticles not associated with the cells. The cells were trypsinized, the trypsin was neutralized with cell culture media, and then the cells were transferred to 1.5 ml microcentrifuge tubes. Half the cells were exposed to an AMF (292 kHz, 56 kA/m) for 1 h. The cells were then reseeded into black walled 96-well plates at 15,000 cells/ml and 100 µl/well and allowed to grow for 48 h prior to staining the cells with 2 µM calcein AMF and reading fluorescence on a plate reader (ex/em: 485/528 nm). Fluorescence was normalized to the fluorescence of the control (no nanoparticles and no AMF treatment).

Statistical analysis

Statistical analysis was completed using SigmaPlot 13.0. A one-way ANOVA was used to determine the statistical differences in the iron oxide nanoparticle uptake study. A two-way ANOVA with an interaction tern was used to analyze all other experiments.

Results & discussion

Iron oxide nanoparticle characterization

Iron oxide nanoparticles were synthesized via a one-pot coprecipitation method using a 2:1 molar ratio of iron salts and 30% ammonium hydroxide as the reducing agent. Figure 2 depicts the subsequent surface functionalization strategy to conjugate the TAT peptide to the nanoparticle surface via EDC/sulfo-NHS crosslinking. Size and zeta potential measurements are summarized in Table 1. The Z-average hydrated diameter of the nanoparticles ranged from 127 nm for the Fe_3O_4 + TAT to 177 nm for the Fe_3O_4 + Dx-ECH in water. The cross-linked dextran coating on the nanoparticle surface stabilizes the nanoparticles at physiological pH by introducing steric interactions and a relatively neutral surface charge, as indicated by the zeta potential [34,48]. The decrease in size between the Fe_3O_4 + Dx-ECH and Fe_3O_4 + TAT is a result of the additional washing steps required to remove unconjugated TAT peptide after the reaction, which also removes loosely attached dextran which was not cross-linked or removed in previous washing steps. The size of these nanoparticle systems is appropriate for cell internalization while being above the cut-off of renal excretion [49,50]. DLS was also completed in cell culture media to gauge nanoparticle sizes during cell culture studies. The nanoparticles were stored suspended in DI water at 4°C, diluted in cell culture media and bath sonicated for 5 min prior to recording DLS measurements over 10 min. The larger size associated with uncoated Fe_3O_4 and Fe_3O_4 + Dx-ECH-Amine nanoparticles in cell culture medium is an indication that agglomeration of the nanoparticles during storage is not easily reversible. In addition, protein adsorption to the nanoparticle surface could cause the nanoparticles to increase in size and agglomerate, but significant changes in nanoparticle stability were not observed. There is a slight increase in size of the Fe_3O_4 + Dx-ECH and Fe_3O_4 + TAT nanoparticles when suspended in cell culture media compared with DI water likely due to protein adsorption. However, the nanoparticles are stabilized by the dextran cross-linked coating and charge repulsion from the TAT peptide which allows the nanoparticles to be easily resuspended upon bath sonication. Distributions of the hydrodynamic diameter of the nanoparticles is provided in the supplemental section. Probe sonication after dilution in cell culture media results in a unimodal distribution of nanoparticle size. Bath sonication was not powerful enough to completely disassociate agglomerated nanoparticles, resulting in wider and some bimodal distributions. The z-averages presented in Table 1 represent the bath sonicated distributions. The increase in zeta potential between the Fe_3O_4 + Dx-ECH-Amine (-7.45 mV) and Fe_3O_4 + TAT (14.8 mV) indicates successful attachment of the TAT peptide to the surface of the nanoparticle [35].

FTIR was also completed on the Fe_3O_4 + Dx-ECH-Amine and Fe_3O_4 + TAT systems to confirm TAT attachment to the surface [51]. As shown in Figure 3A, there are slight changes in the FTIR spectra, most notably a change in the N-H peak at 3300 cm^{-1} indicating a decrease in primary amines in the coating due to conjugation of the TAT peptide using EDC/sulfo-NHS cross-linking. TEM and XRD were used to determine iron oxide crystal size. Example TEM images of the dextran coated iron oxide nanoparticles are shown in Figure 3B. The images shown depict multiple nanoparticle crystals of approximately 8.9 ± 2 nm (average ± standard deviation as determined by ten images at 60 nanoparticles per image) in size encapsulated within the dextran coating. The crystalline size is not expected to change with further functionalization of the surface. XRD (Figure 3C) confirmed the crystalline structure of the nanoparticles to be iron oxide (likely a combination of magnetite and maghemite due to oxidation), and the Scherrer equation (Equation 1) and the (311) peak was used to calculate the average crystal length to be approximately 12.1 ± 0.2 nm (n = 3 individual batches), which is comparable to the crystal length determined via TEM imaging. Although bulk heating was not the focus of this work, the specific absorption rate (SAR) is an indication of how the nanoparticles interact with an AMF. Previous characterization of the cross-linked dextran coated iron oxide nanoparticles indicated a SAR value of 211.0 ± 46.6 W/g (58 kA/m, 292 kHz), confirming the ability of the nanoparticles to respond to an AMF [52].

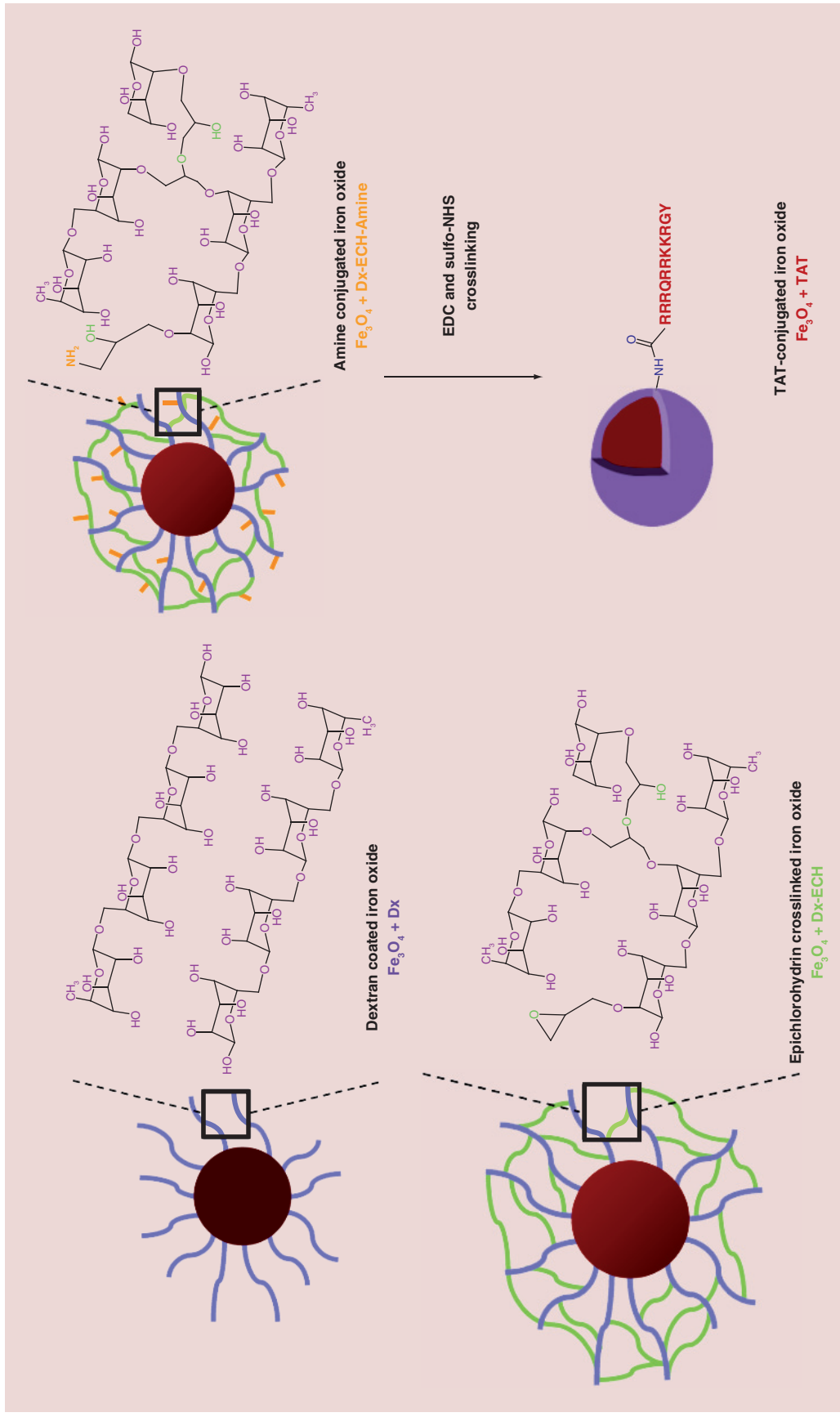

Figure 2. Iron oxide nanoparticle synthesis and functionalization of the TAT peptide. Iron oxide nanoparticles are synthesized coated with dextran. The dextran coating is then cross-linked and functionalized with primary amines which allow for TAT peptide conjugation. The purple shell in the TAT conjugated iron oxide nanoparticle system represents the dextran coating.

Table 1. Iron oxide nanoparticle Z-average size from dynamic light scattering in deionized water and cell culture media and zeta potential represented as average ± standard deviation of three independent samples (n = 3).

Fe_3O_4 nanoparticle system	DI water		DMEM + 10% FBS		Zeta potential (mV)
	Size (nm)	PDI	Size (nm)	PDI	
Uncoated	136.5 ± 1.8	0.2 ± 0.02	355.1 ± 23.2	0.3 ± 0.04	17.3 ± 4.1
Dx-ECH	177.3 ± 3.7	0.1 ± 0.03	203.4 ± 4.8	0.2 ± 0.01	-5.3 ± 3.9
Amine	173.7 ± 1.6	0.1 ± 0.02	405.7 ± 29.0	0.3 ± 0.03	-7.5 ± 6.2
TAT	126.9 ± 3.2	0.2 ± 0.02	201.5 ± 15.1	0.2 ± 0.02	14.8 ± 4.7

DI: Deionized; DMEM: Dulbecco's modified Eagle medium; FBS: Fetal bovine serum; PDI: Polydispersity Index.

Cellular uptake of iron oxide nanoparticles

A549 and H358 lung cancer cells were exposed to three nanoparticle systems of interest at a concentration of 500 µg/ml for 2 h. This exposure time and concentration were kept constant throughout the studies completed. As shown in Figure 4, Fe_3O_4 + TAT uptake was significantly greater than the other nanoparticle systems in both cell lines due to the TAT peptide being a cell penetrating peptide and positively charged, which enhances internalization of its attached cargo [32,36,48,53,54]. The uncoated Fe_3O_4 nanoparticles were internalized to a significantly greater extent than Fe_3O_4 + Dx-ECH in A549 cells and slightly greater in H358 cells. This is likely due to the positive zeta potential associated with uncoated Fe_3O_4 [55]. The Fe_3O_4 + Dx-ECH system did not result in significant uptake, as the iron concentration is not different from that of the control, and this is likely a result of the slightly

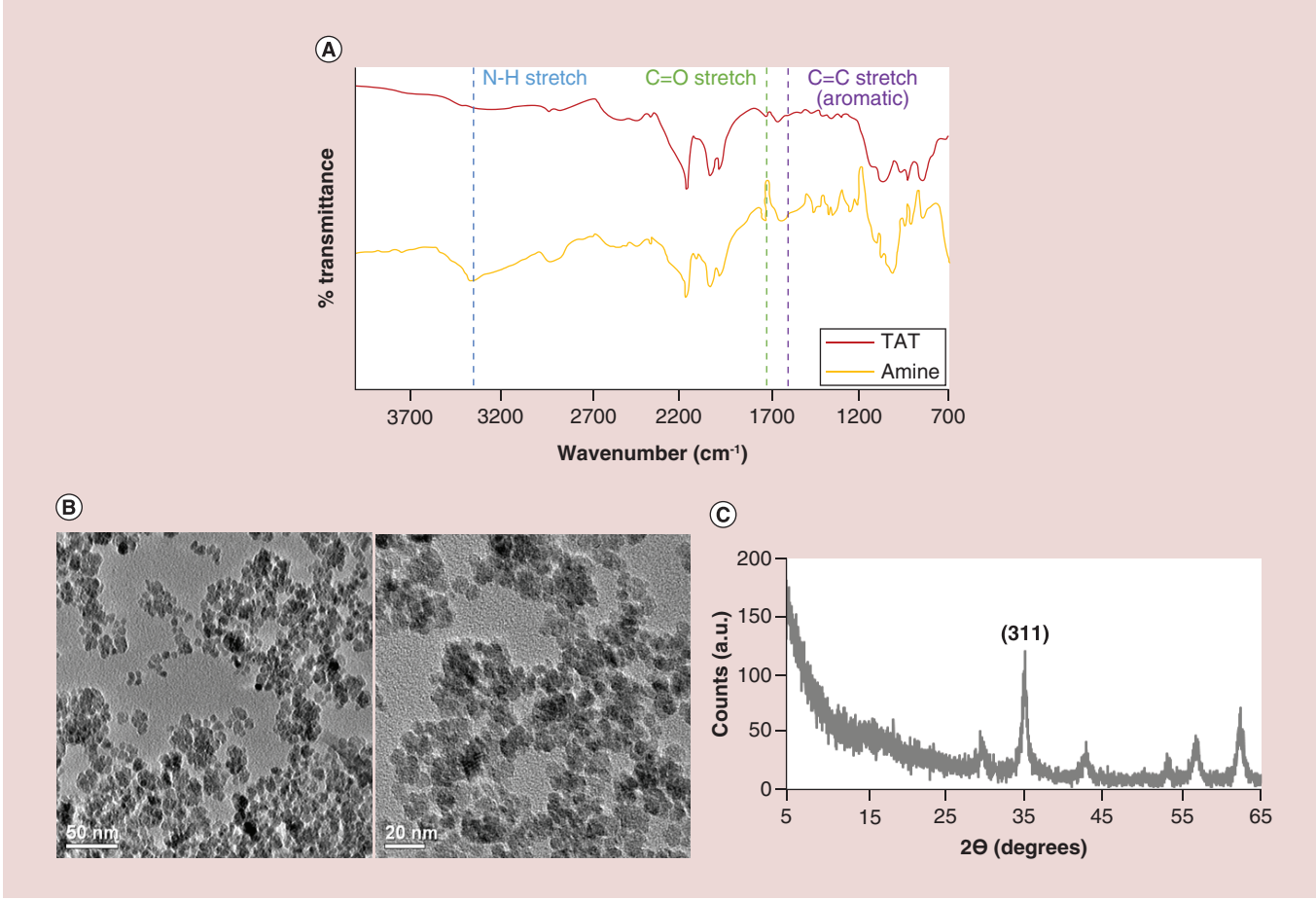

Figure 3. Nanoparticle characterization. **(A)** FTIR spectra of amine functionalized and TAT conjugated iron oxide nanoparticles. **(B)** TEM images of dextran coated iron oxide nanoparticles to confirm Fe_3O_4 crystalline structure. **(C)** X-ray diffraction pattern of dextran coated iron oxide nanoparticles.

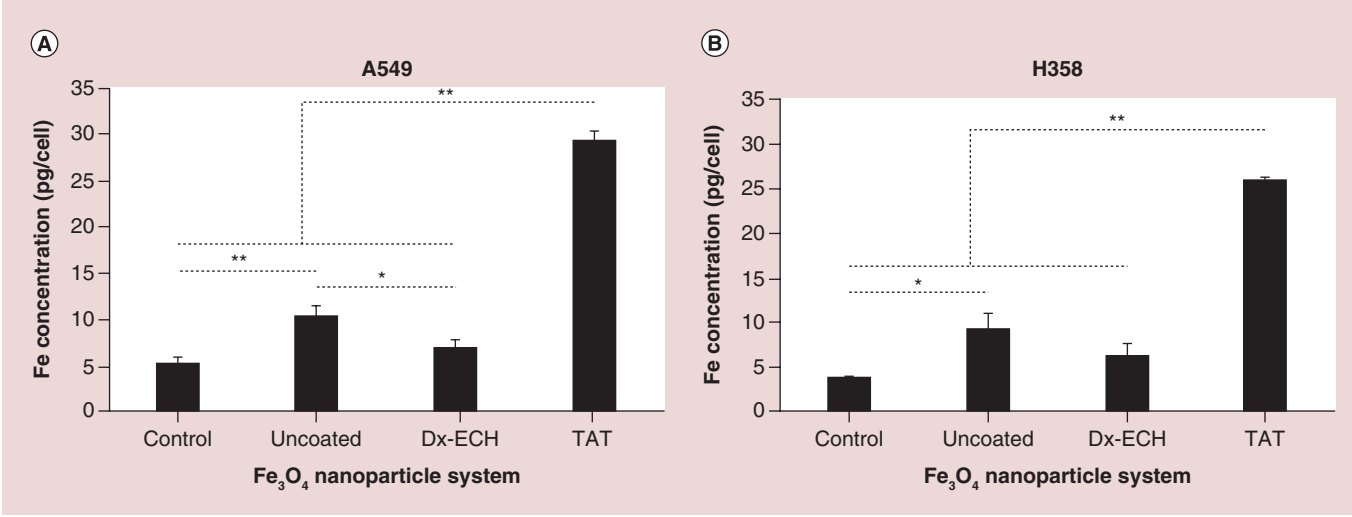

Figure 4. Uptake of Fe_3O_4 nanoparticles into (A) A549 and (B) H358 lung cancer cells. Error bars represent standard error (n = 3) and significant differences are indicated by *p < 0.05 and **p < 0.01 via a one-way ANOVA.

negative surface charge which limits uptake [53]. It was expected that the effects of Fe_3O_4 + TAT nanoparticles in the presence of an AMF will be greater than the other nanoparticle systems studied due to increased intracellular concentrations.

Intracellular ROS formation

Iron oxide nanoparticles have the ability to catalyze the formation of the hydroxyl radical via Fenton chemistry. It has been previously shown that hydroxyl radical formation is enhanced in the presence of an AMF due to energy dissipation by Brownian rotation and Neél relaxation resulting in cellular stress [29]. Figure 5A shows carboxy-DCF fluorescence of A549 lung carcinoma exposed to the three nanoparticle systems and a control followed by 30 min or 1 h AMF treatment, which did not result in a measurable temperature rise. AMF treatment for 30 min significantly enhanced ROS production in A549 cells exposed to uncoated Fe_3O_4 and Fe_3O_4 + TAT. The surface of uncoated Fe_3O_4 is not shielded and therefore can interact with the cell environment and catalyze hydroxyl radical formation through Fenton chemistry. Enhancement of ROS generation via uncoated Fe_3O_4 in the presence

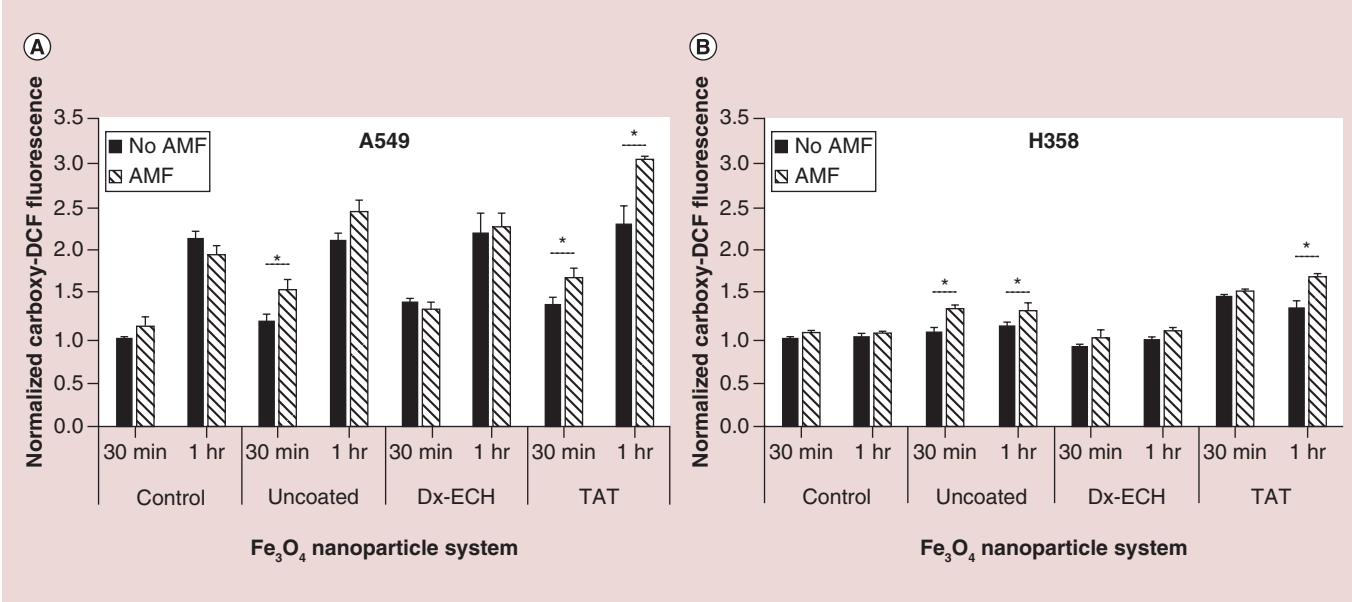

Figure 5. Normalized carboxy-DCF fluorescence of (A) A549 and (B) H358 lung cancer cells after treatment with Fe_3O_4 nanoparticles with and without 30 min or 1 h alternating magnetic field exposure. Error bars represent standard error (n = 3) and significant difference is indicated by *p < 0.05 via a two-way ANOVA.

of an AMF was previously shown by Wydra *et al.* [29], where methylene blue decolorization was enhanced in the presence of uncoated Fe_3O_4 and an AMF compared with the theoretical degradation associated with bulk temperature rise.

Fe_3O_4 + TAT nanoparticles are potentially inducing local heating effects or frictional effects from Brownian rotation and therefore causing cell stress and increasing ROS production. Only the Fe_3O_4 + TAT increased ROS production in A549 lung carcinoma when exposed to an AMF for both 30 min and 1 h, which is likely due to the increased concentration of intracellular nanoparticles and, therefore, greater local heating and frictional effects. Although not significant, uncoated Fe_3O_4 combined with 1 h AMF exposure slightly increased intracellular ROS production. The convergence in ROS production between uncoated Fe_3O_4 and uncoated Fe_3O_4 with 1 h AMF can be explained by the inherent ability of the nanoparticle to increase intracellular ROS production through Fenton chemistry at the surface even without local energy dissipation [29]. The longer AMF exposure time increased the amount of time that the internalized nanoparticles were able to interact intracellularly, which could cause a convergence in ROS generation between the no AMF and 1 h AMF treatments for cells exposed to uncoated Fe_3O_4.

It should also be noted that the A549 control cells, which were not exposed to iron oxide nanoparticles, still generate ROS through natural cellular respiration. By increasing AMF exposure time, carboxy-DCF exposure time also increased resulting in increased fluorescence being associated with the longer AMF exposure. By doubling the AMF exposure time, the carboxy-DCF exposure nearly doubled, resulting in a near twofold increase in fluorescence of control A549 cells. However, this was not observed in H358 cells as shown in Figure 5B. Increased H358 incubation time with carboxy-DCF did not show the same increase in fluorescence indicating that the cells were potentially operating at their maximal ROS generation rate. The difference in inherent ROS production between A549 and H358 cells was determined by incubating the cells with 50 μM carboxy-DCF for 2 h and then measuring the raw fluorescence of the cells via flow cytometry. As shown in Figure 6, H358 cells operated at a higher level of ROS generation than A549 cells. Previous work by Trachootham *et al.* in 2006 showed that increased oxidative stress in cancer cells is associated with oncogenic transformation by transfecting T72 ovarian cells with the Ras gene [56]. Oncogenic transformation resulted in increased oxidative stress as well as increased sensitivity to ROS inducing agents. Therefore, increased oxidative stress results in greater dependence upon antioxidant systems causing the cells to be more sensitive to exogenous agents, which threaten this delicate balance [28,56–58].

Intracellular effects of internalized iron oxide nanoparticles & AMF exposure

There are a multitude of intracellular properties and pathways that can be affected by increased ROS production. Therefore, we have evaluated lysosomal permeability, mitochondrial membrane permeability, apoptosis via the Caspase 3/7 pathway and cell viability of A549 and H358 lung cancer cells after exposure to the nanoparticle systems with and without 1 h of AMF exposure. AMF exposure did not result in a measurable temperature rise.

An increase in lysosome permeability is associated with several apoptosis pathways. Destabilization of

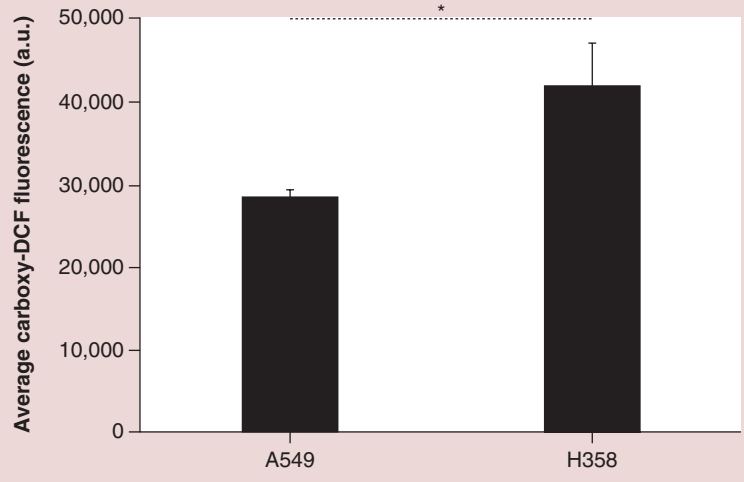

Figure 6. Average fluorescence of A549 and H358 cells after 2 h of exposure to 50 μM carboxy-DCF. Error bars represent standard error (n = 5) and * indicates a significant difference ($p < 0.05$) via a t-test.

the lysosomal membranes releases lysosomal contents such as proteolytic enzymes (e.g., cathepsins) into the cytosol, which then induces mitochondrial damage by enhancing the production of superoxide radicals and hydrogen peroxide, further increasing lysosome permeability, resulting in an amplifying feedback loop [59]. Acridine orange (AO) is a metachromatic fluorophore which gives a distinct red fluorescence at high lysosomal concentrations and a weakly green fluorescence at the low cytosolic concentration and can therefore be used to measure lysosomal membrane permeability, with a decrease in the red fluorescence channel corresponding to an increase in lysosome permeability [60]. AO red fluorescence was measured for A549 (Figure 7A) and H358 (Figure 7B) immediately following iron oxide nanoparticle internalization and 1 h of AMF exposure, and these fluorescence intensities were then normalized to the control with no AMF exposure. Lysosome permeability increased with Fe_3O_4 + TAT treatment in both A549 and H358 cells. However, the permeability was not further increased by AMF exposure. This could be a result of saturating the assay as the Fe_3O_4 + TAT nanoparticles permeabilized the lysosomal membranes to the same extent as the 100 µM hydrogen peroxide positive control (data not shown), and thus, the effects of the AMF could not increase the permeability further. In A549 lung carcinoma, all of the nanoparticles significantly increased lysosome permeability. This could be due to the uncoated Fe_3O_4 nanoparticles generating ROS within the lysosome, leading to destabilization of the membrane [60].

The JC-1 assay employs a cationic dye that exhibits potential dependent accumulation in mitochondria. At high concentrations, such as those in the mitochondria, the JC-1 dye aggregates to form red-fluorescent J-aggregates. Depolarization of the mitochondrial membrane results in lower JC-1 concentrations and therefore the formation of green-fluorescent monomers. Mitochondrial membrane potential can be monitored using the JC-1 ratio (red/green fluorescence). A decrease in the red/green fluorescence ratio is the result of mitochondrial membrane depolarization, which occurs in the early stages of apoptosis [61]. Figure 8 shows the percentage of cells with mitochondrial membrane depolarization, which resulted in a decreased JC-1 ratio. In A549 lung carcinoma, Fe_3O_4 + TAT treatment resulted in a significant increase in the percentage of the cell population with depolarized mitochondrial membranes. However, this was not significantly increased with the addition of AMF treatment. As previously mentioned, mitochondrial integrity can be compromised by increases in lysosomal permeability due to the escape of toxins and proteolytic enzymes into the cytosol. Therefore, it is hypothesized that the Fe_3O_4 + TAT nanoparticles permeabilized the lysosomal membranes which then affected the mitochondrial integrity of the A549 lung carcinoma. There is also the possibility that the Fe_3O_4 + TAT nanoparticles fully escaped the lysosomes, interacting with the mitochondria and catalyzing ROS formation at the mitochondria. However, it should be noted that this effect is cell line dependent as the Fe_3O_4 + TAT nanoparticles did not disrupt the mitochondrial membrane integrity in H358 lung carcinoma.

An increase in lysosome membrane permeability and depolarization of the mitochondrial membrane are both found upstream in many apoptotic pathways [61,62]. Therefore, the effects of the iron oxide nanoparticle

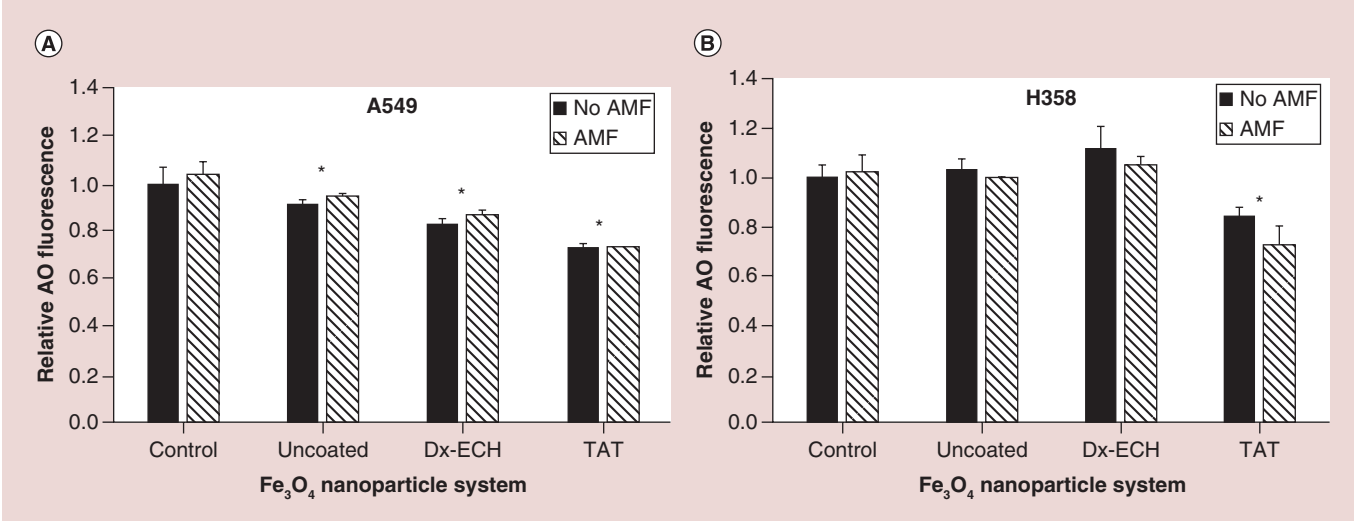

Figure 7. Relative acridine orange (AO) fluorescence of (A) A549 and (B) H358 lung cancer cells after treatment with Fe_3O_4 nanoparticles with and without 1 h alternating magnetic field exposure. Error bars represent standard error (n = 3) and significant difference from the control is indicated by *p < 0.05 via a two-way ANOVA.

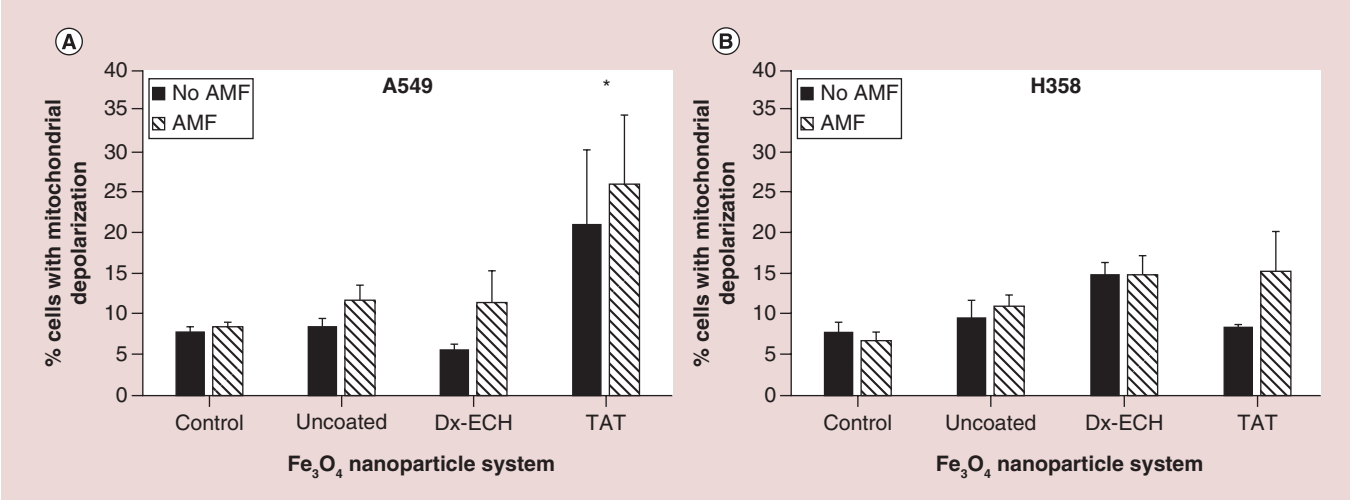

Figure 8. Percentage of (A) A549 and (B) H358 cells with depolarized mitochondrial membranes as indicated by a decrease in the ratio between FL3/FL1 (JC1 ratio). Error bars represent standard error (n = 3) and * indicates a significant difference ($p < 0.05$) compared with the control as determined via a two-way ANOVA.

systems and subsequent AMF exposure on the Caspase 3/7 apoptotic pathway were evaluated. Due to the cells being in different stages of the cell cycle at the time of treatment, the time between treatment and analysis of the apoptotic population was delayed to 12 and 24 h post treatment. These time points were determined using hydrogen peroxide controls and evaluating the peak times of apoptosis following treatment (data not shown). Although there were no statistically significant differences between the percent of apoptotic cells when comparing the nanoparticle systems to one another and the individual systems with and without AMF treatment, there were trends in the data that are interesting and warrant further exploration of these potential effects. In Figure 9, both A549 lung carcinoma and H358 bronchi alveolar appeared to increase in apoptosis when the nanoparticles were combined with AMF, although not significant. Additionally, H358 cells appeared to have increased apoptosis compared with A549 in all treatments. This could be a result of the H358 cells being more sensitive to the treatment as well as the processing procedure of the experiment. It also appeared as though uncoated Fe_3O_4 and Fe_3O_4 + TAT resulted in greater apoptosis than the Fe_3O_4 + Dx-ECH in H358 cells which corresponds to the ROS generation data provided previously. The significant error observed in this assay prevents firm conclusions about differences between the treatments. However, as previously mentioned, there were notable trends in the data. In future studies, additional assays, such as Annexin V/Propid-

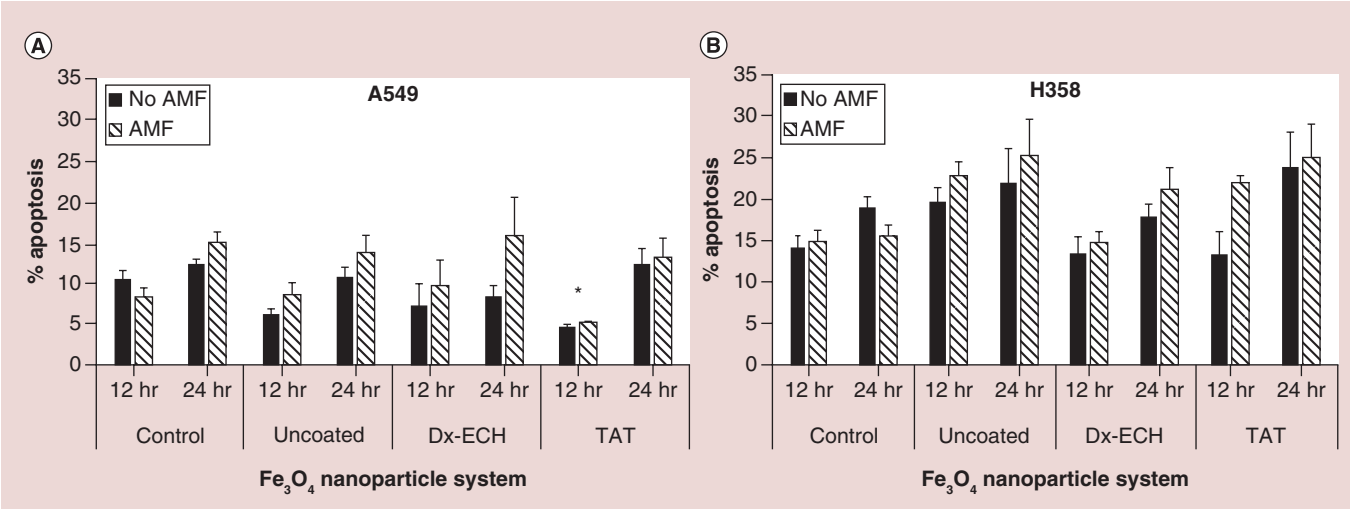

Figure 9. Percentage apoptosis of (A) A549 and (B) H358 lung cancer cells 12 and 24 h after treatment with Fe_3O_4 nanoparticles with and without 1 h alternating magnetic field. Error bars represent standard error (n = 3) and significant difference from the control is indicated by *$p < 0.05$ via a two-way ANOVA.

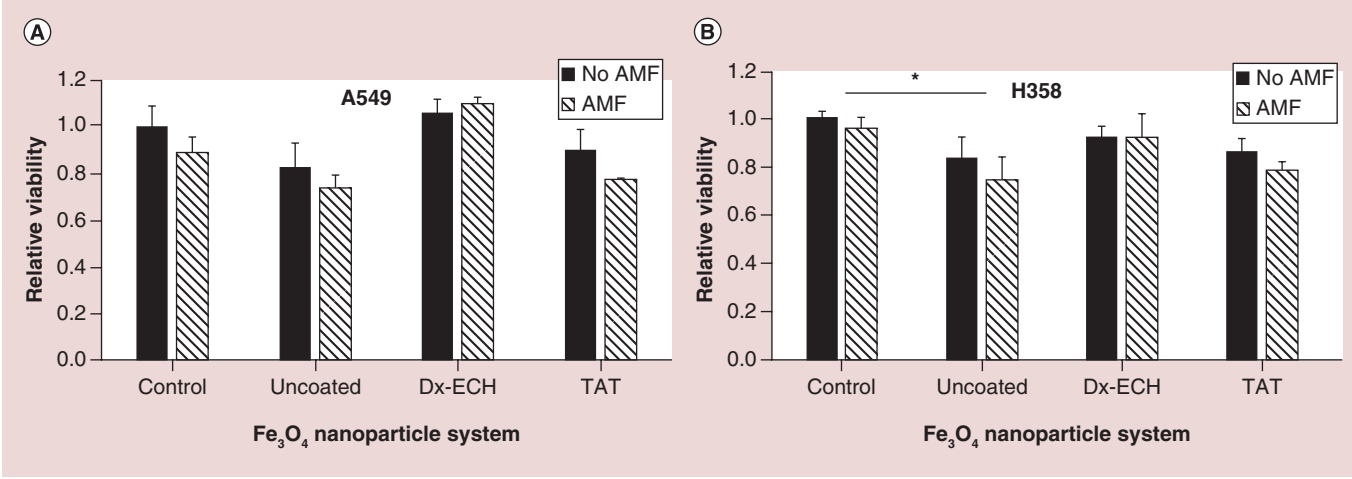

Figure 10. Relative viability of (A) A549 and (B) H358 lung cancer cells 48 h after treatment with Fe_3O_4 nanoparticles with and without 1 h alternating magnetic field. Error bars represent standard error (n = 3) and significant difference from the control is indicated by *p < 0.05 via a two-way ANOVA.

ium iodide (PI), will be used as the variability in the current assay limit the conclusions that can currently be made. Additionally, prior work by Wydra *et al.* used the Caspase 3/7 assay to show a significant increase in apoptosis of CT26 colon cancer cells when uncoated, citric acid coated and glucose functionalized iron oxide nanoparticles were combined with AMF (292 kHz, 56 kA/m) exposure for 1 h compared with the nanoparticle systems alone [47,63]. The effect was larger in this case and found to be statistically significant, which further confirms that the efficacy of MagMED treatment is cell line dependent as expected.

A549 and H358 viability 48 h following treatment with the nanoparticle systems with and without AMF was evaluated and shown in Figure 10. In A549 lung carcinoma, there is no significant difference between the nanoparticle systems and the control or within a nanoparticle system with and without AMF treatment. In the H358 cells, only the uncoated Fe_3O_4 nanoparticles resulted in a decrease in cell viability compared with the control, but there was no additional decrease in viability as a result of AMF treatment. In the apoptosis experiments, specifically in the H358 cells, there is no statistically significant increase in apoptosis of cells exposed to the nanoparticle systems (with or without AMF treatment) compared with the control. Since the percentage of apoptosis is not significantly different between the control and cells exposed to the Fe_3O_4 + TAT nanoparticles, it is not expected that the relative viability would be significantly different between the two treatments. The significant decrease in H358 viability compared with the control associated with uncoated Fe_3O_4 nanoparticles is likely due to the long-term toxicity of the internalized uncoated Fe_3O_4 nanoparticles. Although intracellular effects of the nanoparticle systems combined with AMF were observed (e.g., especially in intracellular ROS generation), the intracellular effects were not enough to induce a decrease in cell viability. Previous work by Creixell *et al.* showed a significant decrease in cell viability when internalized EGFR targeted iron oxide nanoparticles were combined with an AMF for 2 h [14]. However, there was significant toxicity of the EGFR targeted nanoparticles alone which could have sensitized the cells to additional treatment with the AMF. Additionally, the AMF treatment time was 2 h instead of the 1 h used in these studies. Another study completed by Domenech *et al.* demonstrated that intracellular energy delivery is cell line dependent. MDA-MB 231 and 184–85 cells were incubated with EGF targeted, carboxymethyl dextran coated iron oxide nanoparticles and then exposed to an AMF (233 kHz, 41.75 kA/m) for 1 h [64]. A decrease in viability of MDA-MB-231 cells was observed with the addition of AMF treatment while 184–85 cell viability was not affected by AMF treatment. Future work will explore utilizing intracellular energy delivery as a combinational treatment in order to enhance the efficacy of conventional treatments such as chemotherapy and radiation. It is possible that intracellular energy delivery can act as a sensitizer to additional treatments resulting in a synergistic combinational effect.

Conclusion

Dextran coated iron oxide nanoparticles were successfully functionalized with the TAT peptide and characterized for their physicochemical properties. The nanoparticles range in size from approximately 130–180 nm and successful conjugation of the TAT peptide was confirmed by changes in nanoparticle zeta potential and FTIR spectra. TAT functionalization to dextran coated iron oxide nanoparticles resulted in a

novel nanoparticle system in which the nanoparticles were internalized within cells at significantly greater concentrations but were not internalized via receptor-mediated endocytosis. Uncoated Fe_3O_4 and Fe_3O_4 + TAT increased cellular ROS generation in both A549 and H358 cell lines upon exposure to an AMF. Lysosomal permeability was increased in both cell lines following treatment with Fe_3O_4 + TAT nanoparticles due to the TAT peptide destabilizing the lysosomal membranes. In A549 cells, the mitochondrial integrity was compromised by the Fe_3O_4 + TAT nanoparticles but this was not enhanced by AMF exposure or observed in H358 cells, indicating a cell dependent response to treatment. Apoptosis response was also cell line dependent, and although not statistically significant, trends were observed that suggested an increase in apoptosis when nanoparticle systems were combined with AMF treatment. However, there was no difference in the treatments when cell viability was analyzed 48 h post treatment. Future work will aim to increase consistency of apoptosis assays and increase the scope of tested cell lines. Targeting the nanoparticles to specific organelles could also improve the efficacy of MagMED, especially if the particles were targeted to vital organelles such as the mitochondria.

Supplementary data

To view the supplementary data that accompany this paper please visit the journal website at: www.futuremedicine.com/doi/full/10.2217/nnm-2016-0050

Disclaimer

The content is solely the responsibility of the authors and does not necessarily represent the official views of the National Cancer Institute or the National Institutes of Health. Any opinions, findings and conclusions, or recommendations expressed in this material are those of the author(s) and do not necessarily reflect the views of the National Science Foundation.

Financial & competing interests disclosure

The project described was partially supported by grant number R25CA153954 from the National Cancer Institute. Additionally, this work was supported by the National Science Foundation Graduate Research Fellowship Program grant no. DGE-1247392. The authors have no other relevant affiliations or financial involvement with any organization or entity with a financial interest in or financial conflict with the subject matter or materials discussed in the manuscript apart from those disclosed.

No writing assistance was utilized in the production of this manuscript.

Executive summary

- TAT conjugation to iron oxide nanoparticles facilitated increased cellular uptake and resulted lysosomal destabilization following internalization.
- Uncoated and TAT conjugated iron oxide nanoparticles increased cellular reactive oxygen species generation upon exposure to an alternating magnetic field.
- TAT conjugated iron oxide nanoparticles compromised mitochondrial integrity in a cell line dependent manner.
- Trends suggested increased cell apoptosis following treatment with both TAT conjugated iron oxide nanoparticles and an alternating magnetic field.

References

Papers of special note have been highlighted as: • of interest; •• of considerable interest

1 Mccormack PL. Ferumoxytol in iron deficiency anaemia in adults with chronic kidney disease. *Drugs* 72(15), 2013–2022 (2012).

2 Laurent S, Dutz S, Hafeli UO, Mahmoudi M. Magnetic fluid hyperthermia: focus on superparamagnetic iron oxide nanoparticles. *Adv. Colloid Interface Sci.* 166, 8–23 (2011).

3 Hu R, Ma S, Li H *et al.* Effect of magnetic fluid hyperthermia on lung cancer nodules in a murine model. *Oncol. Lett.* 2(6), 1161–1164 (2011).

4 Dennis CL, Jackson AJ, Borchers JA *et al.* Nearly complete regression of tumors via collective behavior of magnetic nanoparticles in hyperthermia. *Nanotechnology* 20(39), 395103 (2009).

5 Plouffe BD, Murthy SK, Lewis LH. Fundamentals and application of magnetic particles in cell isolation and enrichment: a review. *Rep. Progr. Phys.* 78(1), (2015).

6 Min KA, Shin MC, Yu F *et al.* Pulsed magnetic field improves the transport of iron oxide nanoparticles through cell barriers. *ACS Nano* 7(3), 2161–2171 (2013).

7 Kruse AM, Meenach SA, Anderson KW, Hilt JZ. Synthesis and characterization of CREKA-conjugated iron oxide nanoparticles for hyperthermia applications. *Acta Biomater.* 10(6), 2622–2629 (2014).

8 Wydra RJ, Kruse AM, Bae Y, Anderson KW, Hilt JZ. Synthesis and characterization of PEG-iron oxide core-shell composite nanoparticles for thermal therapy. *Mater. Sci. Eng. C Mater. Biol. Appl.* 33(8), 4660–4666 (2013).

9 Rodriguez-Luccioni HL, Latorre-Esteves M, Mendez-Vega J *et al.* Enhanced reduction in cell viability by hyperthermia induced by magnetic nanoparticles. *Int. J. Nanomedicine* 6, 373–380 (2011).

10 Oliveira TR, Stauffer PR, Lee C-T *et al.* Magnetic fluid hyperthermia for bladder cancer: a preclinical dosimetry study. *Int. J. Hyperthermia* 29(8), 835–844 (2013).

11 Wang LF, Dong J, Ouyang WW, Wang XW, Tang JT. Anticancer effect and feasibility study of hyperthermia treatment of pancreatic cancer using magnetic nanoparticles. *Oncol. Rep.* 27(3), 719–726 (2012).

12 Hu RL, Ma SL, Li H *et al.* Effect of magnetic fluid hyperthermia on lung cancer nodules in a murine model. *Oncol. Lett.* 2(6), 1161–1164 (2011).

13 Gordon RT, Hines JR, Gordon D. Intracellular hyperthermia – biophysical approach to cancer-treatment via intracellular temperature and biophysical alterations. *Med. Hypotheses* 5(1), 83–102 (1979).

14 Creixell M, Bohorquez AC, Torres-Lugo M, Rinaldi C. EGFR-targeted magnetic nanoparticle heaters kill cancer cells without a perceptible temperature rise. *ACS Nano* 5(9), 7124–7129 (2011).

•• **EGFR-targeted nanoparticles internalized within a cell induce cell death upon activation by an alternating magnetic field without a bulk temperature rise.**

15 Villanueva A, De La Presa P, Alonso JM *et al.* Hyperthermia HeLa cell treatment with silica-coated manganese oxide nanoparticles. *J. Phys. Chem. C* 114(5), 1976–1981 (2010).

16 Grazu V, Silber AM, Moros M *et al.* Application of magnetically induced hyperthermia in the model protozoan Crithidia fasciculata as a potential therapy against parasitic infections. *Int. J. Nanomedicine* 7, 5351–5360 (2012).

17 Kozissnik B, Bohorquez AC, Dobson J, Rinaldi C. Magnetic fluid hyperthermia: advances, challenges, and opportunity. *Int. J. Hyperthermia* 29(8), 706–714 (2013).

• **Review of magnetically mediated hyperthermia and introduction of magnetically mediated energy delivery.**

18 Rabin Y. Is intracellular hyperthermia superior to extracellular hyperthermia in the thermal sense? *Int. J. Hyperthermia* 18(3), 194–202 (2002).

• **Calculations suggest that nanoscale heating from a single nanoparticle is insufficient to induce cellular damage.**

19 Huang H, Delikanli S, Zeng H, Ferkey DM, Pralle A. Remote control of ion channels and neurons through magnetic-field heating of nanoparticles. *Nat. Nanotechnol.* 5(8), 602–606 (2010).

20 Sanchez C, Diab DEH, Connord V *et al.* Targeting a G-protein-coupled receptor overexpressed in endocrine tumors by magnetic nanoparticles to induce cell death. *ACS Nano* 8(2), 1350–1363 (2014).

21 Connord V, Clerc P, Hallali N *et al.* Real-time analysis of magnetic hyperthermia experiments on living cells under a confocal microscope. *Small* 11(20), 2437–2445 (2015).

22 Johansson A-C, Appelqvist H, Nilsson C, Kagedal K, Roberg K, Ollinger K. Regulation of apoptosis-associated lysosomal membrane permeabilization. *Apoptosis* 15(5), 527–540 (2010).

23 Linder ST, Erdal H, Berndtsson M, Shoshan M. Induction of lysosomal membrane permeabilization by compounds that activate p53-independent apoptosis. *Proc. Natl Acad. Sci. USA* 102(1), 192–197 (2005).

24 Kirkegaard T, Jaattela M. Lysosomal involvement in cell death and cancer. *Biochim. Biophys. Acta Mol. Cell Res.* 1793(4), 746–754 (2009).

25 Jaattela M. Multiple cell death pathways as regulators of tumour initiation and progression. *Oncogene* 23(16), 2746–2756 (2004).

26 Zhang E, Kircher MF, Koch M, Eliasson L, Goldberg SN, Renstrom E. Dynamic magnetic fields remote-control apoptosis via nanoparticle rotation. *ACS Nano* 8(4), 3192–3201 (2014).

27 Kehrer JP. The Haber-Weiss reaction and mechanisms of toxicity. *Toxicology* 149(1), 43–50 (2000).

28 Klein S, Sommer A, Distel LVR, Neuhuber W, Kryschi C. Superparamagnetic iron oxide nanoparticles as radiosensitizer via enhanced reactive oxygen species formation. *Biochem. Biophys. Res. Commun.* 425(2), 393–397 (2012).

29 Wydra RJ, Oliver CE, Anderson KW, Dziubla TD, Hilt JZ. Accelerated generation of free radicals by iron oxide nanoparticles in the presence of an alternating magnetic field. *RSC Adv.* 5(24), 18888–18893 (2015).

30 Austin LA, Kang B, Yen CW, El-Sayed MA. Nuclear targeted silver nanospheres perturb the cancer cell cycle differently than those of nanogold. *Bioconjug. Chem.* 22(11), 2324–2331 (2011).

31 Pan LM, He QJ, Liu JN *et al.* Nuclear-targeted drug delivery of TAT peptide-conjugated monodisperse mesoporous silica nanoparticles. *J. Am. Chem. Soc.* 134(13), 5722–5725 (2012).

32 Wang C, Qiao L, Zhang Q, Yan H, Liu K. Enhanced cell uptake of superparamagnetic iron oxide nanoparticles through direct chemisorption of FITC-Tat-PEG(600)-b-poly(glycerol monoacrylate). *Int. J. Pharm.* 430(1–2), 372–380 (2012).

33 Josephson L, Tung CH, Moore A, Weissleder R. High-efficiency intracellular magnetic labeling with novel superparamagnetic-tat peptide conjugates. *Bioconjug. Chem.* 10(2), 186–191 (1999).

34 Lewin M, Carlesso N, Tung CH *et al.* Tat peptide-derivatized magnetic nanoparticles allow *in vivo* tracking and recovery of progenitor cells. *Nat. Biotechnol.* 18(4), 410–414 (2000).

35 Rao KS, Reddy MK, Horning JL, Labhasetwar V. TAT-conjugated nanoparticles for the CNS delivery of anti-HIV drugs. *Biomaterials* 29(33), 4429–4438 (2008).

36 Torchilin VP. Tat peptide-mediated intracellular delivery of pharmaceutical nanocarriers. *Adv. Drug Deliv. Rev.* 60(4–5), 548–558 (2008).

37 De La Fuente JM, Berry CC. Tat peptide as an efficient molecule to translocate gold nanoparticles into the cell nucleus. *Bioconjug. Chem.* 16(5), 1176–1180 (2005).

38 Oyelere AK, Chen PC, Huang X, El-Sayed IH, El-Sayed MA. Peptide-conjugated gold nanorods for nuclear targeting. *Bioconjug. Chem.* 18(5), 1490–1497 (2007).

39 Vives E, Brodin P, Lebleu B. A truncated HIV-1 Tat protein basic domain rapidly translocates through the plasma membrane and accumulates in the cell nucleus. *J. Biol. Chem.* 272(25), 16010–16017 (1997).

40 Xu C, Xie J, Kohler N, Walsh EG, Chin YE, Sun S. Monodisperse magnetite nanoparticles coupled with nuclear localization signal peptide for cell-nucleus targeting. *Chem. Asian J.* 3(3), 548–552 (2008).

41 Yang C, Neshatian M, Van Prooijen M, Chithrani DB. Cancer nanotechnology: enhanced therapeutic response using peptide-modified gold nanoparticles. *J. Nanoscie. Nanotechnol.* 14(7), 4813–4819 (2014).

42 Palmacci S, Josephson L. Synthesis of polysaccharide covered superparamagnetic oxide colloids. United States patent. 5262176 (1993).

43 Singh A, Greninger P, Rhodes D *et al.* A gene expression signature associated with "K-Ras addiction" reveals regulators of EMT and tumor cell survival. *Cancer Cell* 15(6), 489–500 (2009).

44 Sinthupibulyakit C, Ittarat W, St. Clair WH, St. Clair DK. p53 protects lung cancer cells against metabolic stress. *Int. J. Oncol.* 37(6), 1575–1581 (2010).

45 Song L, Morris M, Bagui T, Lee FY, Jove R, Haura EB. Dasatinib (BMS-354825) selectively induces apoptosis in lung cancer cells dependent on epidermal growth factor receptor signaling for survival. *Cancer Res.* 66(11), 5542–5548 (2006).

46 Shintani Y, Maeda M, Chaika N, Johnson KR, Wheelock MJ. Collagen I promotes epithelial-to-mesenchymal transition in lung cancer cells via transforming growth factor-β signaling. *Am. J. Respir. Cell Mol. Biol.* 38(1), 95–104 (2008).

47 Wydra RJ, Rychahou PG, Evers BM, Anderson KW, Dziubla TD, Hilt JZ. The role of ROS generation from magnetic nanoparticles in an alternating magnetic field on cytotoxicity. *Acta Biomater.* 25, 284–290 (2015).

•• **Uncoated, citric acid capped and glucose coated iron oxide nanoparticles induced apoptosis in CT26 colon cancer cells upon activation by an alternating magnetic field. It is suspected that the increase in apoptosis is due to an increase in intracellular ROS generation.**

48 Ayala V, Herrera AP, Latorre-Esteves M, Torres-Lugo M, Rinaldi C. Effect of surface charge on the colloidal stability and *in vitro* uptake of carboxymethyl dextran-coated iron oxide nanoparticles. *J. Nanopart. Res.* 15(8), 1874 (2013).

49 Ogawara K, Yoshida M, Higaki K *et al.* Hepatic uptake of polystyrene microspheres in rats: effect of particle size on intrahepatic distribution. *J. Control. Release* 59(1), 15–22 (1999).

50 Petters C, Bulcke F, Thiel K, Bickmeyer U, Dringen R. Uptake of fluorescent iron oxide nanoparticles by oligodendroglial OLN-93 cells. *Neurochem. Res.* 39(2), 372–383 (2014).

51 Li Z, Dong K, Huang S *et al.* A smart nanoassembly for multistage targeted drug delivery and magnetic resonance imaging. *Adv. Funct. Mater.* 24(23), 3612–3620 (2014).

52 Hauser AK, Mathias R, Anderson KW, Hilt JZ. The effects of synthesis method on the physical and chemical properties of dextran coated iron oxide nanoparticles. *Mater. Chem. Phys.* 160, 177–186 (2015).

53 Villanueva A, Canete M, Roca AG *et al.* The influence of surface functionalization on the enhanced internalization of magnetic nanoparticles in cancer cells. *Nanotechnology* 20(11), 115103 (2009).

54 Thorek DLJ, Tsourkas A. Size, charge and concentration dependent uptake of iron oxide particles by non-phagocytic cells. *Biomaterials* 29(26), 3583–3590 (2008).

55 Osaka T, Nakanishi T, Shanmugam S, Takahama S, Zhang H. Effect of surface charge of magnetite nanoparticles on their internalization into breast cancer and umbilical vein endothelial cells. *Colloids Surf. B Biointerfaces* 71(2), 325–330 (2009).

56 Trachootham D, Zhou Y, Zhang H *et al.* Selective killing of oncogenically transformed cells through a ROS-mediated mechanism by beta-phenylethyl isothiocyanate. *Cancer Cell* 10(3), 241–252 (2006).

57 Huang G, Chen HB, Dong Y *et al.* Superparamagnetic iron oxide nanoparticles: amplifying ROS stress to improve anticancer drug efficacy. *Theranostics* 3(2), 116–126 (2013).

58 Wang J, Yi J. Cancer cell killing via ROS To increase or decrease, that is the question. *Cancer Biol. Ther.* 7(12), 1875–1884 (2008).

59 Zhao M, Antunes F, Eaton JW, Brunk UT. Lysosomal enzymes promote mitochondrial oxidant production, cytochrome c release and apoptosis. *Eur. J. Biochem.* 270(18), 3778–3786 (2003).

60 Terman A, Kurz T, Gustafsson B, Brunk UT. Lysosomal labilization. *Iubmb Life* 58(9), 531–539 (2006).

61 Ly JD, Grubb DR, Lawen A. The mitochondrial membrane potential (Delta psi m) in apoptosis; an update. *Apoptosis* 8(2), 115–128 (2003).

62 Brunk UT, Neuzil J, Eaton JW. Lysosomal involvement in apoptosis. *Redox Rep.* 6(2), 91–97 (2001).

63 Hauser AK, Wydra RJ, Bhandari R *et al.* Corrigendum to "The role of ROS generation from magnetic nanoparticles in an alternating magnetic field on cytotoxicity". *Acta Biomater.* 25, 284–290 (2015).

64 Domenech M, Marrero-Berrios I, Torres-Lugo M, Rinaldi C. Lysosomal membrane permeabilization by targeted magnetic nanoparticles in alternating magnetic Fields. *ACS Nano* 7(6), 5091–5101 (2013).

•• **Targeted magnetic nanoparticles increase lysosomal membrane permeability upon activation by an alternating magnetic field, resulting in increased cell apoptosis.**